

From theory to practice: Hybrid Modeling and experimental insights into a pinion-double-rack system

1st Santiago Estrada Bernal 
Programa de Ingeniería Mecatrónica
Universidad EIA
Envigado, Colombia
santiago.estrada6@eia.edu.co

2nd María Camila Tonuzco 
Programa de Ingeniería Mecatrónica
Universidad EIA
Envigado, Colombia
maria.tonuzco@eia.edu.co

3rd Tatiana Manrique 
Dep. Mecatrónica y Electromecánica
Institución Universitaria ITM
Medellín, Colombia
dollymanrique@itm.edu.co

Abstract—This work presents the modeling and control-oriented analysis of a pinion-double-rack mechanism as a hybrid dynamical system (HDS). The system integrates continuous electromechanical dynamics with discrete switching behavior, making it a compelling case study for hybrid control strategies. A state-space model is derived from first principles, incorporating both electrical and mechanical subsystems, and extended into a hybrid automaton framework with mode transitions governed by rack displacement thresholds. Experimental validation is conducted using a custom-built setup featuring a DC motor, current sensing, and encoder-based feedback. Friction effects are experimentally identified and modeled to enhance simulation fidelity. Comparative analysis between simulated and experimental results demonstrates strong agreement in dynamic trajectories and validates the hybrid automaton-based model. Additionally, energy consumption analysis highlights the efficiency gap between ideal and real-world implementations. This study underscores the relevance of hybrid modeling in precision control applications and provides a foundation for future work in hybrid control design and optimization.

Index Terms—Hybrid systems, electromechanical devices, nonlinear control systems, experimental validation, system identification.

I. INTRODUCTION

The modeling and control of electromechanical systems with nonlinear and switching dynamics present significant challenges in both theoretical formulation and practical implementation. Traditional continuous-time models often fall short in capturing the full behavior of systems that exhibit discrete transitions, such as those caused by mechanical limits, friction, or control logic. In such cases, hybrid dynamical systems (HDS) provide a robust framework by integrating continuous dynamics with discrete events, enabling a more accurate representation of real-world behavior. This paper focuses on the hybrid modeling and experimental validation of a pinion-double-rack mechanism—a system characterized by bidirectional motion, spring interactions, and discrete switching based on positional constraints. While the system can be described analytically using state-space methods and hybrid automata, the presence of nonlinearities such as friction and inertia-induced overshoot necessitates empirical validation to ensure model fidelity.

To bridge the gap between theoretical modeling and physical behavior, a data-driven approach is incorporated into the hybrid modeling process. This integration enhances the model's ability to reflect real-world dynamics by leveraging experimental data to refine system parameters and validate switching conditions. However, this approach introduces its own set of challenges, including the need for high-quality, high-resolution data and the mitigation of sensor noise and environmental variability. Ensuring that the collected data is both sufficient in quantity and reliable in quality is essential for meaningful model refinement. Despite these challenges, the benefits of a data-driven hybrid modeling approach are substantial. By grounding the model in empirical observations, the resulting representation captures subtle nonlinear behaviors and system uncertainties that are often overlooked in purely analytical models. This leads to improved simulation accuracy, more robust control strategies, and deeper insight into the system's hybrid nature.

This work presents a comprehensive methodology for modeling, simulating, and experimentally validating a pinion double-rack system as a hybrid dynamical system. The results demonstrate the effectiveness of combining theoretical modeling with data-driven refinement to achieve a high-fidelity representation of complex electromechanical systems. The paper organizes as follows: First, it begins with an extensive review of related works in Sect. II, focusing on the applications and relevance of the pinion-double-rack mechanism. This is followed by a study on hybrid automata to model the pinion-double-rack system. In Sec. III, the mathematical modeling of the pinion-double-rack system is carried out using differential equations, which are then reformulated into a state-space model. The system's hybrid automaton is defined, and the experimental setup is also described. Subsequently, Sec. IV presents the data acquisition process and the results obtained, including friction identification, the implementation of the hybrid automaton, and its contribution to improving the model. Additionally, a comparison of energy consumption is conducted. Finally, the conclusions are presented in Sec. V.

II. RELATED WORKS

Hybrid automata offer a formal framework for systems with discrete transitions, making them useful in mechanical systems with impacts, friction, or switching. Applications include multi-rigid-body interactions [1] and multi-contact systems with friction and impacts modeled through Newton's impact law and Coulomb friction [2]. Hybrid models have also been applied in wave energy harvesting, where [3] used state-dependent mass modulation with experimental validation, showing how switching surfaces defined by system constraints improve efficiency. Their methodology parallels the present work, which defines switching surfaces in a double-rack and pinion system using preset maximum distances. Similarly, [4] introduced a constrained hybrid controller that partitions the state space into regions with distinct dynamics, enabling optimal graph-based control. This strategy is relevant for managing transitions in partitioned hybrid models. In power electronics, [5] used a hybrid automaton in a photovoltaic system, combining inner-loop switching control with outer-loop PI and MPPT regulation. A broader overview of hybrid system methods is given by [6], highlighting their utility for systems with multiple operating modes.

Rack-and-pinion mechanisms remain central in applications converting rotation to translation [7]–[10]. Historically, they enabled industrial gripping devices [8]. More recent designs include a dual rack-and-pinion for automotive window lifts, which improves efficiency and reduces weight [11], and a double-rack single-pinion in roll forming machines, where predefined positional constraints ensure operation within limits [12], similar to the switching surfaces in this study. Precision has been advanced by dual-motor preload control for backlash reduction in machine tools [7]. In energy harvesting, [9] modeled a rack-and-pinion system with a one-way clutch using separate mechanical and electrical equations, later validated experimentally. This mirrors the modeling methodology of the present research. Finally, rack-and-pinion control has been applied in electric power steering, where [10] developed a state-space controller addressing delays and nonlinearities, illustrating the adaptability of these mechanisms in modern control systems.

III. SYSTEM DESCRIPTION

The pinion-double-rack system with springs consists of two opposing racks separated by a gear. The gear, driven by an electric motor, enables the vertical motion of each rack, which is mechanically connected to an identical spring at its base. The springs are assumed to have the same stiffness. According to the control law, the gear moves in one direction until the upward-moving rack reaches a predefined limit, determined by the physical constraints of the system and encoded in the control logic. Upon reaching this limit, the direction reverses, allowing the opposite rack to move upward until it reaches the same height. Both racks are of equal length. The variables of interest are the angular displacement $\theta(t)$ [rad], which is proportional to the displacement of each rack, the angular velocity $\omega(t)$ [$\frac{\text{rad}}{\text{s}}$], and the DC motor current I_a [A].

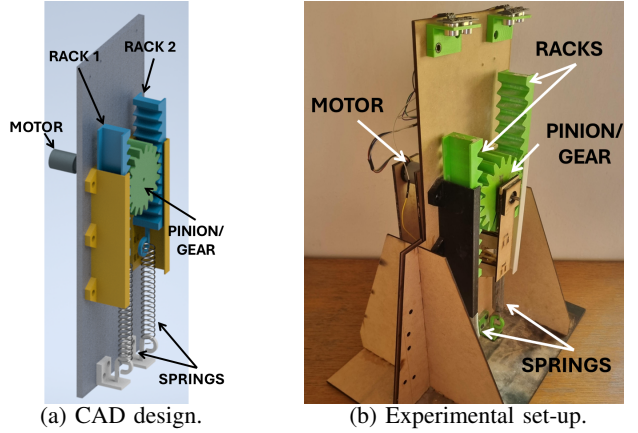


Fig. 1: Pinion-double-rack system.

A. Dynamic Analysis

In a pinion-double-rack system, when the pinion rotates clockwise, rack 1 moves upward and rack 2 moves downward. Conversely, when the pinion rotates counterclockwise, rack 2 moves upward while rack 1 moves downward. The physical modeling of this system can be established through a set of differential equations that describe both the electrical and mechanical dynamics of the system. This includes applying Kirchhoff's voltage law to the DC motor armature, deriving torque balance equations from Newton's second law, and modeling spring torques as a function of deformation. The model simplifies the system by neglecting the mass of the racks—since their influence is minimal—and assuming perfect coupling between the racks and the gear.

The torque produced by each spring acting on the gear can be expressed as $T_1(t) = T_2(t) = R\delta(t)K_i$, where $T_1(t)$ and $T_2(t)$ [Nm] are the torques exerted by the respective rack's spring, R [m] is the radius of the gear, $\delta(t)$ [m] is the scalar displacement of each rack from its equilibrium position, and K_i [$\frac{\text{N}}{\text{m}}$] is the stiffness constant of the i -th spring, with $i \in \{1, 2\}$. These expressions were derived based on Hooke's law, which models the elastic force opposing deformation.

Building upon that foundation, the present work reformulates the system using a state-space approach, which allows for more effective simulation, control design, and integration into hybrid modeling frameworks. The electromechanical model shown in Fig. 1a consists of a DC motor, two symmetrically opposed racks, and linear springs that will be treated.

The motor model follows the typical electrical diagram for a DC motor [13], leading to the voltage equation (1), where $V_{in}(t)$ [V] is the input voltage, $V_{R_a}(t)$ [V] and $V_{L_a}(t)$ [V] are the voltages of the armature resistance and inductance, respectively, and $V_M(t)$ [V] is the motors electromotive force. Notice that the voltage $V_{in}(t)$ is the element that allows the system to change direction, becoming negative once the control law states that the gear must inversely rotate.

$$0 = V_{in}(t) - V_{R_a}(t) - V_{L_a}(t) - V_M(t) \quad (1)$$

This leads to (2), assuming K_e [$\frac{\text{Vs}}{\text{rad}}$] as the voltage

constant, which is proportional to the angular velocity of the motor $\omega(t)$ [$\frac{\text{rad}}{\text{s}}$]. The variable of interest is $I_a(t)$ [A].

$$\dot{I}_a(t) = \frac{1}{L_a} V_{in}(t) - \frac{R_a}{L_a} I_a(t) - \frac{K_e}{L_a} \omega(t) \quad (2)$$

Newton's second law on the pinion yields (3), where J [Nms²] is rotational inertia, and $T_M(t)$ [Nm] is the motor's moment.

$$J\ddot{\omega}(t) = T_M(t) - T_2(t) - T_1(t) \quad (3)$$

With the torque expressions substituted, $T_M(t) = K_t I_a(t)$, and taking K_t [$\frac{\text{Nm}}{\text{A}}$] as the motor torque constant, the angular acceleration becomes (4):

$$\ddot{\omega}(t) = \frac{K_t}{J} I_a(t) - \delta(t) \left(\frac{RK_2 + RK_1}{J} \right) \quad (4)$$

The rack displacement is directly related to angular velocity as described by (5), where $\dot{\delta}(t)$ [$\frac{\text{m}}{\text{s}}$] is the rack's linear velocity.

$$\dot{\delta}(t) = R\dot{\theta}(t) = R\omega(t) \quad (5)$$

State-space representation is a fundamental technique for analyzing dynamic systems, particularly in mechanical modeling of gears, racks, and springs [14]. Prior work has explored state-space methods for representing mechanical systems with mass-spring-damper configurations and external excitations [15]. These models provide the foundation for analyzing electromechanical systems and are particularly relevant for systems that exhibit hybrid or switching dynamics. The state space of the system can be formulated in the form $\dot{X}(t) = AX(t) + BU(t)$, where $X(t) = [I_a(t) \ \omega(t) \ \delta(t)]^T$ is the state vector and $U(t)$ is the input vector, which will only contain $V_{in}(t)$. This results in (6).

$$\dot{X}(t) = \begin{bmatrix} -\frac{R_a}{L_a} & -\frac{K_e}{L_a} & 0 \\ \frac{K_t}{J} & 0 & -\frac{RK_2+RK_1}{J} \\ 0 & R & 0 \end{bmatrix} \begin{bmatrix} I_a(t) \\ \omega(t) \\ \delta(t) \end{bmatrix} + \begin{bmatrix} \frac{1}{L_a} \\ 0 \\ 0 \end{bmatrix} V_{in}(t) \quad (6)$$

The formulation of a state space facilitates simulation and output extraction. The $y(t)$ vector, which contains the output, was chosen with the variables that could be measured later through sensors and whose information was valuable. For this reason, $y(t) = X(t)$. The output equation is $y(t) = CX(t) + DU(t)$, expanded in (7).

$$y(t) = \begin{bmatrix} \theta(t) \\ \omega(t) \\ I_a(t) \end{bmatrix} = \begin{bmatrix} 0 & 0 & \frac{1}{R} \\ 0 & 1 & 0 \\ 1 & 0 & 0 \end{bmatrix} \begin{bmatrix} I_a(t) \\ \omega(t) \\ \delta(t) \end{bmatrix} + \mathbf{0}_{(3 \times 1)} V_{in}(t) \quad (7)$$

B. Hybrid automaton modeling

The hybrid model was implemented by defining a sextuple $(Q, X(t), D(q), f(q_1, X(t)), E, G)$ [16]. Two separate states were considered to implement control over this system following the movements described as in Section III-A. The displacement variable $\dot{\delta}(t)$ was taken to be divided into two new states for rack 1, $\dot{x}_1(t)$ which describes a movement to the upside and $\dot{x}_2(t)$ that describes a movement to the

downside. This new modeling conserves the representation obtained in (6) whenever the movement is upward, where $\dot{X}(t) = A_1 X(t) + B_1 U(t)$. To explain the system going downward the same mathematical model was performed as in $\dot{X}(t) = A_2 X(t) + B_2 U(t)$, and it was obtained that $B_1 = -B_2$ and $A_1 = -A_2$. With this in mind, the hybrid automaton is defined as follows:

1) *Set of modes Q*: $Q = \{q_1, q_2\}$, with mode q_1 representing the upwards movement of rack 1, and q_2 representing downwards movement of rack 1.

2) *State space*: $X(t) \in \mathbb{R}^3, X(t) = [I_a(t) \ \omega(t) \ \delta(t)]^T$.

3) *Domains*: $D(q_1) = \{X(t) \in \mathbb{R}^3 : I_a(t) \in \mathbb{R}^+, w(t) \in \mathbb{R}^+, -2\pi \cdot 0.15 \leq \delta(t) < 2\pi \cdot 0.15\}$. This domain describes the continuous values taken by $X(t)$ while operating in mode 1.

$D(q_2) = \{X(t) \in \mathbb{R}^3 : I_a(t) \in \mathbb{R}^-, w(t) \in \mathbb{R}^-, -2\pi \cdot 0.15 < \delta(t) \leq 2\pi \cdot 0.15\}$. This domain describes the continuous values taken by $X(t)$ while operating in mode 2.

4) *Flow functions*: $f(q_1, X(t)) = A_{q_1} X(t) + B_{q_1} U(t)$, as a linear function whose values depend on matrices A_Q and B_Q , according to modes Q.

$$f(q_2, X(t)) = A_{q_2} X(t) + B_{q_2} U(t)$$

5) *Set of edges*: $E = \{(q_1, q_2), (q_2, q_1)\}$.

6) *Set of Guards*: When $\delta(t) = 2\pi \cdot 0.15$ the transition from mode q_1 to mode q_2 will occur, therefore the guard for this transition can be defined as: $G(q_1, q_2) = [I_a(t) \in \mathbb{R}^+, w(t) \in \mathbb{R}^+, \delta(t) = 2\pi \cdot 0.15]$ When $\delta = -2\pi \cdot 0.15$ the transition from mode q_2 to mode q_1 will occur, therefore the guard for this transition can be defined as: $G(q_2, q_1) = [I_a(t) \in \mathbb{R}^+, w(t) \in \mathbb{R}^+, \delta(t) = -2\pi \cdot 0.15]$

7) *Reset map*: When the system transitions from one mode to another, the velocity is assumed to be conserved, but inverted. The reset map is defined as follows: $R(q_1, q_2, X(t)) = [I_a(t) \in \mathbb{R}^+, w(t) \in \mathbb{R}^+, -2\pi \cdot 0.15 \leq \delta(t)]$

$$R(q_2, q_1, X(t)) = [I_a(t) \in \mathbb{R}^-, w(t) \in \mathbb{R}^-, \delta(t) \leq 2\pi \cdot 0.15]$$

The final model of the HDS can be seen in Fig. 2.

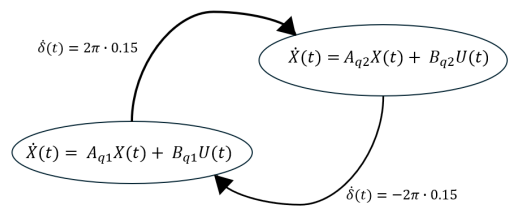


Fig. 2: HDS Pinion-double-rack system.

C. Experimental setup

Establishing the numerical values of each parameter was essential for the simulation. Several experiments were carried out to characterize the springs and the DC motor, the explanation of which is outside the scope of this paper. The parameters used are depicted in Table I.

The electronic components used include the following sensors and actuators: **i) ACS 712 Current Sensor**: The ACS712 is a Hall effect-based linear current sensor with 2.1 kV_{RMS}

TABLE I: Parameter values and units.

Parameter	Value	Units
R	49.5×10^{-3}	m
M	0.39645	kg
J	4.857×10^{-4}	Nms ²
K_e	1.1459	Vs/rad
K_t	0.01819	Nm/A
La	18.138	H
Ra	2.59×10^2	Ω
K_1	0.8682	N/m
K_2	0.8682	N/m

voltage isolation and an integrated low-resistance current conductor. Essentially, current measurement is performed using its built-in conductor. Key features include an 80kHz bandwidth, an output sensitivity ranging from 66 to 185 $\frac{mV}{A}$, a low-noise analog signal path, and an adjustable bandwidth through the FILTER pin. It has an internal conductor resistance of 1.2 mΩ, a total output error of 1.5% at 25°C, stable output offset voltage, and near zero magnetic hysteresis; *ii) Pololu 37D Metal Gearmotor:* This reference has a gear ratio of 102.08:1 and an integrated 64 CPR quadrature encoder was used to generate the movement of the system and record the angular displacement of the gear simultaneously; *iii) Microcontroller:* An ArduinoUNO microcontroller was in charge of handling the information provided by all sensors and sending the values separated by commas to the serial port. A .csv file was thus created from this information to be examined using Matlab. Velocities were obtained through discrete derivatives. This means that two values of displacement were subtracted and the result was divided by the sampling time, which was chosen to be 50ms. The code is available upon request; *iv) H-Bridge L293D:* The L293D motor driver IC was interfaced with the ArduinoUNO to control the motor's direction by switching the polarity of the output voltage supplied to the motor.

The real-life configuration of the system is shown in Fig. 1b. To ensure structural stability, a more robust support was added. The microcontroller, current sensor, H-bridge, and DC motor are located on the back of the structure, while ultrasonic sensors are mounted on the front. However, the built-in encoder was used to measure displacement because of its lower signal noise compared to the ultrasonic sensors.

IV. EXPERIMENTAL RESULTS AND DISCUSSION

The simulation was conducted in MATLAB® and its Simulink® add-on, using a fixed time step of 50 ms, based on the diagram depicted in Fig. 3. The input to the system was a step voltage, while the outputs are defined as shown in (7). Notably, the function block labeled MatrixSelector receives two inputs: spring deformation $\delta(t)$ and the system's input $U(t) = V_{in}(t)$. This block outputs $B_1U(t)$ or $B_2U(t)$, enabling the system to switch and reverse its direction.

A. Friction experimental identification

The simulated behavior was compared to the experimental results. Fig. 4 illustrates the angular displacement $\theta(t)$ (in radians) for both the initial simulation and the experimental

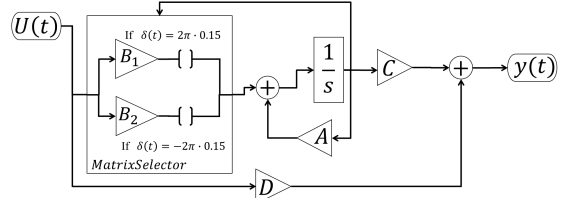


Fig. 3: Pinion-double-rack dynamics.

results. The delay observed in the experimental results relative to the simulation, as well as the difference in the period, suggests the presence of a force impeding the system's free motion. This force was identified as friction, modeled as viscous friction for simplicity because of its linear nature. Consequently, the gear's angular velocity now exhibits a direct dependence on itself, resulting in a modified state matrix A , as shown in (8), where b represents the viscous friction coefficient.

$$\begin{bmatrix} -\frac{R_a}{L_a} & -\frac{K_e}{L_a} & 0 \\ \frac{K_t}{J} & -\frac{b}{J} & -\frac{RK_2+RK_1}{J} \\ 0 & R & 0 \end{bmatrix} \quad (8)$$

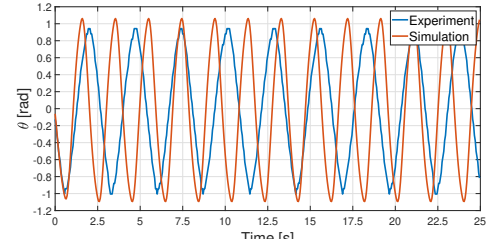


Fig. 4: Initial angular displacement in simulation and experiment.

Given the operating magnitudes of the system, the viscous friction coefficient, expressed in $\frac{Nm}{rad}$, was estimated to be within the range of 5×10^{-4} to 1×10^{-3} . An iterative process was then initiated to identify the specific coefficient value that best aligned the simulation with the observed real-world behavior. The angular displacement was selected as the focus variable for this comparison because of the high reliability of the encoder used in the measurements.

The Mean squared error (MSE) metric was used to determine the optimal value of the viscous friction coefficient b . A lower MSE value indicates a better alignment between the model and/or simulation and the observed data, reflecting a more accurate representation of the underlying phenomenon. Table II presents the MSE values obtained by applying different friction coefficients in the simulation. A noticeable improvement in MSE was observed as the coefficient increased from 0.0007 $\frac{Nm}{rad}$ to 0.00077 $\frac{Nm}{rad}$. However, further increasing the coefficient to 0.0008 $\frac{Nm}{rad}$ resulted in a higher MSE compared to the previous iteration. Therefore, the optimal friction coefficient was determined to be the value corresponding to the penultimate iteration.

Fig. 5 presents a comparison between the experimental and newly simulated angular displacements. As anticipated, the superposition of the two curves demonstrates a higher degree of similarity after incorporating the identified viscous

TABLE II: Mean squared error values for angular displacement with different viscous friction coefficients.

Viscous Friction Coefficient b [$\frac{\text{Nm}}{\text{rad}}$]	MSE
0	0.967789
0.0007	0.259338
0.00073	0.206222
0.00077	0.1092605
0.0008	0.1092945

friction coefficient. Both curves exhibit comparable maximum and minimum values and evolve over time with a similar period, indicating improved alignment between the simulation and the experimental observations. To ensure that selecting b based on the angular displacement did not compromise the accuracy of the approximations for the other two variables of interest (i.e., angular velocity and current), the corresponding MSE values before and after applying the identified viscous friction are presented in Table III. The results indicate that the experimental and modeled values exhibit greater resemblance, confirming the effectiveness of the selected coefficient.

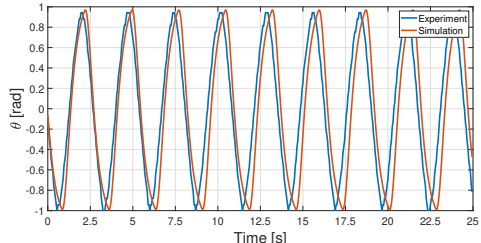


Fig. 5: Angular displacement in simulation with $b = 7.7 \times 10^{-4} \frac{\text{Nm}}{\text{rad}}$ and experiment.

TABLE III: Mean squared error values for angular velocity and current before and after implementing identified viscous friction.

Variable	Initial MSE	Final MSE
Angular velocity ($\omega(t)$)	9.85806	1.20610
Current ($I_a(t)$)	0.034934	0.016469

B. Phases

The pinion double-rack hybrid dynamic system, modeled as described in Section III, switches modes based on a binary command that depends solely on the deformation of the springs, $\delta(t)$, which is indirectly measured through the angular displacement of the gear, $\theta(t)$. Consequently, the system is expected to exhibit immediate transitions when it reaches either of the two imposed guards. Fig. 6 illustrates the relationship between $\theta(t)$ and the angular velocity $\omega(t)$, showing that both the experimental and simulated results reach nearly identical maximum and minimum values, with a magnitude of $2\pi \cdot 0.15$. These values are the guards $G(q_1, q_2)$ and $G(q_2, q_1)$. In particular, the real-life system demonstrates varying angular velocities for nearly the same angular displacement, resulting in a more flattened trajectory. The simulation starting point $X(0)$ is also visible in Fig. 6.

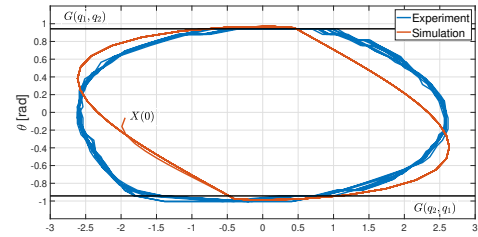


Fig. 6: Experimental and simulated dynamics of pinion double-rack system.

Fig. 7 presents the simulated dynamics of the three key variables of interest: current, angular displacement, and angular velocity, along with the 3D switching surfaces (or guards) $G(q_1, q_2)$ and $G(q_2, q_1)$. A distinct path for the flow functions $f(\delta(\theta(t), q_1))$ and $f(\delta(\theta(t), q_2))$ is clearly visible, as expected due to the noiseless and ideal nature of the simulation. Discrete changes appear at the corners, indicating discontinuities, and consequently, mode transitions.

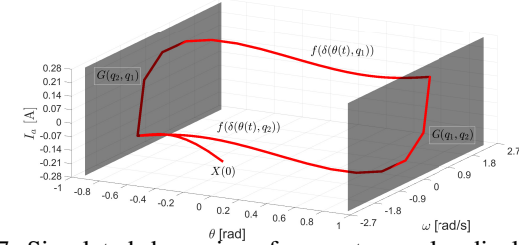


Fig. 7: Simulated dynamics of current, angular displacement, and angular velocity on pinion double-rack system.

Alternatively, Fig. 8 shows the experimental dynamics of the system with the imposed guards. The presence of noise is evident, as reflected by the absence of a unique trajectory for the flow functions $f(\delta(\theta(t), Q))$. Sudden current changes are more pronounced. Additionally, it is important to note that, overall, the current does not transition as smoothly from positive to negative as seen in the simulated results. This is a direct consequence of the real-life motor characteristics, which poses electrical uncertainty, where small current variations do not immediately influence the motor's performance. In addition, noise, voltage variations directly from the source, and mechanic uncertainties of the pinion double-rack system affect global behavior.

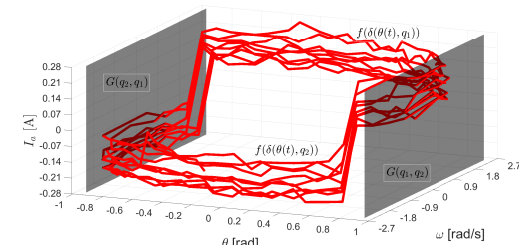


Fig. 8: Experimental dynamics of $I_a(t)$, $\omega(t)$, and $\delta(t)$.

Both the simulated and experimental results do not immediately switch when a guard is reached. This is because the control law does not reduce the velocity as the objective approaches. As a result, the racks and pinions reach maxi-

mum or near-maximum velocity when the direction change is triggered. The inertia of the system causes the gear to exceed the limit before it is fully stopped and reversed. Overall, the simulated and experimental results support that the pinion double-rack system displays continuous and discrete dynamics with clear guards, i.e., it is a hybrid dynamical system

C. Energy Consumption

The energy consumption of an electrical system can be determined by calculating the integral of the system's power with respect to time, as $E = \int_a^b P(t) dt$. Here, E [J] represents the energy consumed over the time interval $[a, b]$ in seconds, and $P(t)$ [W] is the time-dependent function that represents the power of the system. Since the input voltage remained constant throughout the experiment, the equation simplifies to $E = V_{in} \int_a^b |I_a(t)| dt$, where V_{in} denotes the applied voltage and $I_a(t)$ represents the current as a function of time. It must be noticed that the current can take negative values. This, however, does not mean there is a production of energy. Hence, to properly obtain the energy consumed, the absolute value of $I_a(t)$ must be taken. As indicated in Table I, the voltage used was 25% of the nominal value, regulated through a PWM signal generated by an ArduinoUNO. Consequently, the RMS voltage was calculated for a 25% duty cycle, yielding $V_{RMS} = 12 \times \sqrt{0.25} = 6$ V.

The integral was computed numerically using the trapezoidal rule, i.e. $\hat{E} = V_{RMS} \times T_S \sum_{k=1}^N \frac{|y_{k-1} + y_k|}{2}$. In this equation, \hat{E} [J] represents the approximated energy, T_S [s] denotes the sampling time, N is the total number of samples, and y_k [A] corresponds to the k -th sample. Using a sampling time of 50 ms and a total duration of 24.95 s (i.e., 500 samples), the energy consumption was calculated for both the experimental and simulated cases. Fig. 9 illustrates the experimental and simulated currents over time. The experimental current exhibits a slightly shorter period, resulting in a displacement that becomes increasingly pronounced as time progresses. Overall, the energy consumed by the simulation was 16.496 J, whereas the physical setup consumed 21.582 J, representing a 30.83% increase compared to the simulation. This difference can be attributed to the experimental setup not reducing the current to near-zero values after each direction change as effectively as the simulation did.

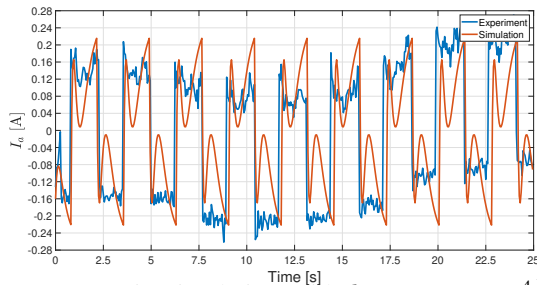


Fig. 9: Current in simulation with $b = 7.7 \times 10^{-4} \frac{\text{Nm}}{\text{rad}}$ and experiment.

V. CONCLUSIONS

This work demonstrated the effective integration of hybrid modeling and experimental validation for a pinion–double-

rack electromechanical system. By combining state-space representations with hybrid automata, the model captured both continuous and discrete behaviors, including switching imposed by mechanical constraints, while a data-driven refinement reduced quadratic error by compensating for nonlinearities such as viscous friction. Rigorous definition of system boundaries enabled implementation of control code that met operating conditions, and experimental validation confirmed the hybrid nature of the system, with clear mode transitions and the influence of inertia and friction. Energy analysis revealed discrepancies between idealized simulations and real behavior, underscoring the importance of empirical validation in control-oriented modeling. Overall, the study highlights the advantages of hybrid automaton frameworks enriched with experimental data and points toward adaptive control and real-time identification as promising directions for improving accuracy and performance.

REFERENCES

- [1] E. Navarro-López and M. O'Toole, "Automated generation of hybrid automata for multi-rigid-body mechanical systems and its application to the falsification of safety properties," *Mathematical and Computer Modelling of Dynamical Systems*, vol. 24, no. 1, pp. 44–75, 2018.
- [2] E. M. Navarro-López and M. D. O'Toole, "A hybrid automaton for a class of multi-contact rigid-body systems with friction and impacts," in *Proceedings of the 4th IFAC Conference on Analysis and Design of Hybrid Systems*, (Eindhoven, The Netherlands), pp. 299–306, 2012.
- [3] C. A. Diamond, C. Q. Judge, B. Orazov, and Ö. Savaş, "Mass-modulation schemes for a class of wave energy converters: Experiments, models, and efficacy," *Ocean Engineering*, vol. 104, pp. 452–468, 2015.
- [4] A. Taghavian, A. Safi, and E. Khammirza, "Constrained computational hybrid controller for input affine hybrid dynamical systems," *Journal of the Franklin Institute*, vol. 361, p. 107142, 2024.
- [5] Z. Hekss, A. Abouloifa, J. Janik, I. Lachkar, S. Echali, F. Chaoui, and F. Giri, "Hybrid automaton control of three phase reduced switch shunt active power filter connected photovoltaic system," *IFAC PapersOnLine*, vol. 53, no. 2, pp. 12847–12852, 2020.
- [6] W. Heemels, D. Lehmann, J. Lunze, and B. De Schutter, "Introduction to hybrid systems," *Handbook of Hybrid Systems Control—Theory, Tools, Applications*, vol. 2, 2009.
- [7] A. Verl and V. Leipe, "Dual motor position feedback control for electrically preloaded rack-and-pinion drive systems to increase accuracy," *CIRP Annals*, 2024.
- [8] F. Y. Chen, "Gripping mechanisms for industrial robots: an overview," *Mechanism and Machine Theory*, vol. 17, no. 5, pp. 299–311, 1982.
- [9] J. Mi, Q. Li, M. Liu, X. Li, and L. Zuo, "Design, modelling, and testing of a vibration energy harvester using a novel half-wave mechanical rectification," *Applied Energy*, vol. 279, p. 115726, 2020.
- [10] V. Govender, L. Ortmann, and S. Müller, "Synthesis and validation of a rack position controller for an electric power steering," in *IFAC-PapersOnLine*, vol. 50, pp. 253–258, IFAC, 2017.
- [11] D. A. Choby, G. J. Jager, J. Johnstone, and P. J. Fenelon, "An efficient light weight all plastic dual rack and pinion window lift mechanism for automotive vehicles," tech. rep., SAE Technical Paper, 2004.
- [12] S. Wenting, L. Qiang, and Q. Bo, "Control strategy for the flexible roll forming machine with the structure of double rack and single gear," in *2011 International Conference on Transportation, Mechanical, and Electrical Engineering (TSEE)*, pp. 2062–2065, IEEE, 2011.
- [13] W. J. Palm, *System dynamics*, vol. 2. McGraw-Hill New York, 2010.
- [14] L. Miková, A. Gmíterko, and D. Hroncová, "State space representation of dynamical systems," *American Journal of Mechanical Engineering*, vol. 4, no. 7, 2016.
- [15] F. A. Shah and A. S. Khan, "Vibrational analysis and optimization of a 2-dof mass spring damper system," *ResearchGate*, 2024.
- [16] T. Manrique and D. Patiño, "Mathematical modelling on hybrid dynamical systems: An application to the bouncing ball and a two-tanks system," in *2010 IEEE ANDESCON*, pp. 1–8, IEEE, 2010.